Article

JOURNAL OF COMPOSITE MATERIALS

Journal of Composite Materials
2018, Vol. 52(7) 953–962

DOI: 10.1177/0021998317717596
journals.sagepub.com/home/jcm
SAGE

# Preparation and characterization of paraffin/nickel foam composites as neutron-shielding materials

**Yun Zhang[1], Feida Chen[1], Xiaobin Tang[1,2], Hai Huang[1], Minxuan Ni[1] and Tuo Chen[1]**

**Abstract**

Traditional neutron-shielding materials usually have poor mechanical properties and secondary gamma-shielding capability. The new requirements of modern neutron-shielding materials are difficult to satisfy. A paraffin/nickel foam neutron-shielding composite was prepared and characterized in this study. Open-cell nickel foams were fabricated through electrodeposition. Subsequently, the paraffin/nickel foam composite were prepared by filling the open-cell nickel foams with melted paraffin. The intrinsic parameters of nickel foam and the content of neutron absorber (boron carbide) were controlled to optimize the composite. The mechanical properties of the composite were studied through a static compression test. The compressive strength improved to 0.4 times that of the nickel foams. The Am–Be source transmittance experiment showed that the 8 cm thick PFM presented a neutron transmittance of 56.1%, and the 6 cm thick boron carbide/paraffin/nickel foam (PFM-B) presented a neutron transmittance of 37.6%. The paraffin/nickel foam and PFM-B had approximately the same shielding efficiency as paraffin and boron carbide/paraffin, respectively. However, the second gamma ray shielding efficiency of the paraffin/nickel foam and PFM-B was significantly higher than that of paraffin and boron carbide/paraffin. The mechanical properties and secondary gamma ray-shielding capability of the composite can be improved by increasing the relative density of nickel foams.

**Keywords**

Paraffin, boron carbide, nickel foams, composite, neutron shielding

## Introduction

Neutron-related technology processes have great applications in our modern society, such as medical treatment, advanced materials analysis, neutron imaging and especially in the nuclear energy industry. It brings us conspicuous convenience but also puts the public into the potential threat of the subsequent neutron radiations.[1,2] Therefore, it is a crucial issue for us to seek more effective ways to confine the neutron radiation to specified region in the nuclear facilities and attenuate the radiation level to a safe range in our daily working places. The neutron radiation shielding materials play a vital role in this regard.

Based on knowledge of the interaction between neutron and materials, the ideal neutron-radiation shielding materials should contain both low atomic number (low-Z) elements (i.e. C, H), high neutron capture cross-section elements (i.e. B, Gd) and high atomic number (high-Z) elements (i.e. Pb, W). First, the energy of neutron radiations drops from dozens of mega electron-volt (MeV) to several MeV through inelastic scattering between neutrons and high-Z-element atoms. Then, the moderated neutrons are moderated further through elastic scattering with low-Z-element atoms and absorbed by high neutron capture cross-section elements. Meanwhile, the secondary $\gamma$-rays are attenuated by high-Z-element components.

[1]Department of Nuclear Science & Engineering, Nanjing University of Aeronautics and Astronautics, Nanjing, China
[2]Jiangsu Key Laboratory of Nuclear Energy Equipment Materials Engineering, Nanjing, China

The first two authors contributed equally to this work.

**Corresponding author:**
Xiaobin Tang, Jiangsu Key Laboratory of Nuclear Energy Equipment Materials Engineering, Nanjing 210016, China.
Email: tangxiaobin@nuaa.edu.cn

Therefore, borated polyethylene, borated paraffin and mixtures of hydrogenous polymers with heavy metal powders and boron compounds are commonly used as neutron radiation-shielding materials.[3–8] However, since their poor mechanical properties and circumscribed thermo-physical characteristics, these traditional polymer composites are unsuitable to be applied in the advanced nuclear facilities, which require the neutron radiation-shielding materials to be lightweight and possess good mechanical properties, long-term reliability, good integrated shielding capability, and joining properties with suitable thermo-physical characteristics.[9]

Metal foams are known for their low density and high strength properties.[9–14] With the view of radiation shielding, it also can be used as the first order neutron-moderator compound and the secondary γ-rays-absorber, as mentioned above. Meanwhile, the open-cells formed inside the metal foams provide natural container for the second-order neutron-moderator polymer compounds and neutron absorber. Therefore, the metal foam/polymer composites are supposed to be a potential advanced neutron radiation-shielding materials which possess integrated shielding capability and good mechanical properties. Furthermore, since the metal foam matrix provides structural support for the polymer, thermal stability of the composites is expected to be significantly improved than the traditional polymer composites. In the previous studies, Chen et al. discussed the feasibility of metal foam composites as neutron-radiation shielding materials.[15,16] In the experiments, the open-cell Al foams were filled with water, borated water and polyethylene, respectively. Their thermal neutron (0.025 eV) and gamma radiation-shielding capabilities were characterized to provide useful insights into the correlation between neutron-shielding effectiveness and metal foams.

In the present work, we designed and prepared a novel kind of paraffin/nickel foam (PFM) neutron-shielding composites. The influence of structural parameters (i.e. pore density, relative density, etc.) of the multiple PFM and boron carbide/paraffin/nickel (PFM-B) foams on the radiation-shielding performance and mechanical properties were studied further. In the composites, nickel foams have a high Z value and good secondary γ-ray-shielding capability. Paraffin is characterized by low-molecular weight, low melt viscosity, and good wettability, which is expected to be a suitable filler for open-cell metal foams. Neutron-absorbing boron carbide ($B_4C$) powder (30 wt.%) was dispersed in paraffin. Considering that the neutron-shielding rate of 0.025 eV neutron does not fully represent the neutron-radiation shielding performance, the shielding experiments were carried out on the Am–Be neutron source and the Monte Carlo particle transportation simulation was utilized to compare and verify the experimental results.

## Materials and method

### Material and sample preparation

*Nickel foam preparation.* The main process of producing nickel foams via the electrodeposition technique includes conductive treatment, electrodeposition, and heat treatment of foams.[17] Heat treatment removes polyurethane foams and recrystallizes nickel. In this work, the heat treatment is ignored to simplify the preparation procedure. Before the conductive treatment, preprocessing procedures were performed on polyurethane foams (Daye Tengfei Sponge Factory, Changzhou, China). Polyurethane foams were cut into a size of 300 mm × 200 mm × 20 mm and placed in a stainless steel container. Next, the foams were dipped into a degreasing solution for 30 min of ultrasonic treatment and into a roughing solution for 1 min. The foams were then rinsed with distilled water and dried. Afterwards, the conductive graphite colloid coating technique was used for conductive treatment. Graphite colloid (HX-10, Qindao Heng Xing Co., Ltd, China) was impregnated into the polyurethane foams for 20 min of ultrasonic treatment and then squeezed out and dried. The polyurethane foams were positioned in the middle of two anodes. Deposition was conducted at a constant current of 2 A $dm^{-2}$ by using a DC power supply. The polyurethane foams had the thickness and porosity of the final product. Different deposition times were selected to obtain the corresponding relative density. Further details on the procedures and production conditions applied in this study are shown in Table 1. All chemicals were from Nanjing Chemical Reagent Co., Ltd (China).

*Preparation of PFM and PFM-B composite.* The impregnation treatment for PFM and PFM-B involved melting–filling and melting–mixing–filling, respectively. For PFM, first, solid paraffin was cut into a size of 200 mm × 200 mm × 10 mm and placed in a stainless steel container. Second, the container was heated in a hot water bath at a constant temperature of 100°C. When the paraffin completely melted into fluid, a piece of metal foam was dipped in it. Third, the paraffin was impregnated into the porous space of the nickel foams completely, and the heating process lasted for about 20 min. Fourth, the stainless steel container was cooled in a cold water at a constant temperature of 25°C for 120 min. Finally, the open-cell nickel foams impregnated with the paraffin were removed, and the

**Table 1.** Production procedures and conditions for continuous nickel foams.

| Procedure | Solution composition and operation conditions |
|---|---|
| Degreasing solution | $Na_2CO_3$ 20–30 g $l^{-1}$ |
| | $Na_3PO_4$ 10–30 g $l^{-1}$ |
| | NaOH 10–20 g $l^{-1}$ |
| | OP-10 0.5 ml $l^{-1}$ |
| | Ultrasonic waves, frequency = 28 kHz |
| Polyurethane foam coarsening | $H_2SO_4$ 13 ml $l^{-1}$ |
| | $KMnO_4$ 7 g $l^{-1}$ |
| Nickel electrodeposition | $NiSO_4$ $6H_2O$ 250–300 g $l^{-1}$ |
| | $NiCl_2$ $6H_2O$ 30–50 g $l^{-1}$ |
| | $H_3BO_3$ 30–50 g $l^{-1}$ |
| | pH 3.5–4.5 |
| | T 45–55°C |
| | Ultrasonic waves, frequency = 48 kHz |

surplus paraffin captured by the surface of the composite was carefully removed.[18]

For PFM-B, after the paraffin completely melted at 100°C, $B_4C$ (30 wt.%) was proportionally added to the paraffin. Surface treatment of carbide boron and nickel foams was done at 5 wt.%. trimethoxyvinylsilane (A-151, China Huaian heyuan Chemical Co., Ltd). The container was removed from the water and stirred at 300 n/min for 3 min at 60°C. Three small samples (1 ml) of mixture were taken out from the container and measured in an analytical balance. This step was repeated until the density of small samples remains stable at 1.35 g/cm$^3$. Afterwards, metal foams and the mixture of paraffin and $B_4C$ were immediately placed in a stainless steel container. The container was shaken to drive air out of the metal foams. The subsequent steps were similar to those for PFM; the only difference is that the cooling medium was ice water. $B_4C$ exhibits good wettability in paraffin but is disturbed by subsidence. Thus, the length of the step involving stirring at 60°C was extended until appropriate viscosity was reached in order to obtain a high impregnation ratio and homogeneous dispersion of $B_4C$. The $B_4C$ came from China Jilin Dunhua Zhengxing Abrasive Co., Ltd. The average size of $B_4C$ used in this investigation was 5 μm. The concentration of B-10 in $B_4C$ is natural abundance.

*Characterization.* The two main parameters of nickel foams are pore density and relative density. Pore density refers to pores per inch (PPI), and relative density is defined as the ratio of the mass density of the cellular material to that of pure nickel.[17]

$$\rho^* = \frac{\rho_{foam}}{\rho_{Ni}},\ \rho_{Ni} = 8900\,\mathrm{kg/m^3} \tag{1}$$

where $\rho_{foam}$ refers to the ratio of nickel foams' mass and volume.

$$\alpha = \frac{m_{actual}}{m_{ideal}} = \frac{m_c - m_{foam}}{(1-\rho^*)\rho_{filler} V_c} \tag{2}$$

The dimensionless parameter impregnation ratio α shown in equation (2) was applied to evaluate the compatibility between the metal foams and fillers.[18] In the equation, $\rho_{filler}$ is the density of solid-state paraffin and boride paraffin, $V_c$ is the volume of the composite, and $m_c$ is the mass of the composite. $\alpha$ reflects the actual mass of filler impregnated into the porous metal foams to the ideal mass that can be impregnated.[17] The value is 100% if all the porous spaces are perfectly impregnated with the filler. The picture of samples were snapped by a mobile phone camera (Vivo 7×).

The mechanical properties of the PFM and PFM-B composites were characterized through static compression tests. The samples have been loaded in compression using two flat platens at a strain rate of 1.2 mm/min and temperature from about 23 to 26°C in a mechanical testing machine (WANCE ETM-105D).[18–20] Grease was applied to the compression platen surface that would press against the specimen.[21] The compression experiment was repeated three times for each specimen.

The Am–Be neutron source was used for the neutron transmission tests. The source was placed at the end of the cylindrical window-oriented detector side in the paraffin box. The cylindrical window was 130 mm deep and 110 mm wide. Neutron ray penetrated through a 30 mm thick lead plate, passed through a polyethylene plate (30 mm thick) and PFM or PFM-B composite samples, and detected with an He-3 proportional counter.[22] A schematic of the neutron shielding performance test is shown in Figure 1(a).

Neutron shielding is unavoidably accompanied by photon flux. For example, photon rays are directly created by the source or a neutron–gamma (n, γ) reaction when shielding materials capture thermal neutrons. Detecting secondary gamma photons directly is difficult because the neutrons could damage and disturb the gamma photon detector system. Hence, the secondary gamma-shielding performances of the PFM and PFM-B composite samples were measured under different gamma-ray irradiation point sources (PU-238 (43 keV, 99 keV, 152 keV), Cs-137 (662 keV)) by using an HPGe

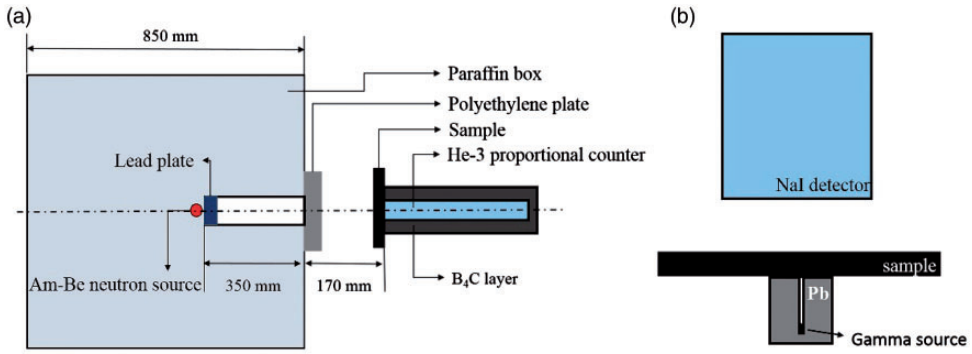


**Figure 1.** Schematic of (a) neutron shielding performance test and (b) photon shielding performance test.

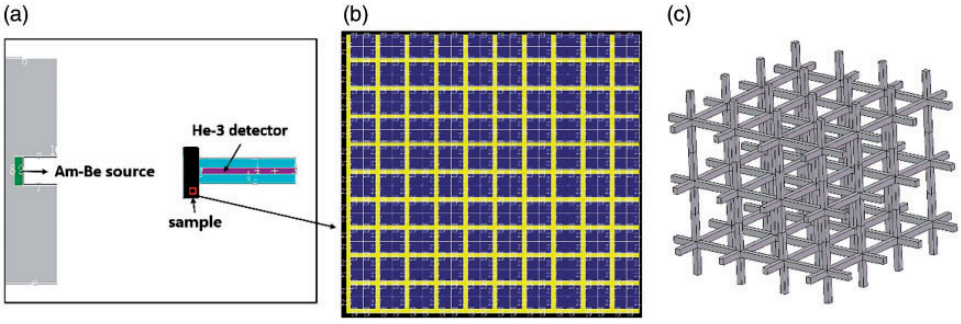


**Figure 2.** (a) Model geometries of neutron shielding performance simulation, (b) model geometries of open-cell Ni foams, and (c) representations of open-cell Ni foams.

detector (ORTEC).[22] The thickness of measured samples was 2 cm. A schematic of the experiment device is shown in Figure 1(b).

*Simulation of shielding performance.* A simulation was performed to test the accuracy of the experimental results. The simulation was conducted with MCNP5, which was developed by Los Alamos National Laboratory. The MCNP code is based on the Monte Carlo method, which can realistically describe random events and calculate the particle transport problem. The simulation geometry setup was similar to that in the experiment. Figure 2(a) shows the cross-section on the YZ plane of the geometry modeling with the MCNP5 code. Tally F4 was used to obtain simulation data. This tally scores the neutron flux in the detector cell. Tally FM4 was used to model the He-3 proportional counter. All the data obtained by MCNP5 were reported with less than 1% error.

Owing to the geometrical complexity and random orientation of the solid phase of the porous medium, the real geometry of foams is unpractical for modeling unless geometric idealization is employed by using a periodic unit cell.[15] Figure 2(b) and (c) shows the simplified model developed in this study. Figure 2(b) shows an enlarged local section of nickel foams modeled on the YZ plane in MCNP. Figure 2(c) shows the 3D microstructure of the open-cell nickel foam model. The experimental and theoretical results of the simplified model exhibit reasonable agreement.

## Results and discussion

### *Structural parameters of samples*

Figure 3(a) and (b) shows the morphologies of the nickel foams before impregnation. The distribution and scatter of pore size of nickel foams are shown in Figure 4. For 12 PPI nickel foam, 85% of pore size are distributed in the range 1.8 mm–2.4 mm. For 6 PPI nickel foam, 66% of pore size are distributed in the range 3.5 mm–4.1 mm. Thus, the distribution of pore size is locally non-uniform but homogeneous as a whole. The average pore size of 6 PPI (pores per inch) and 12 PPI specimens are about 4 and 2 mm, respectively. Pure paraffin is completely compatible with the metal foams, as shown in Figure 3(d) and (e). However, a small quantity of unfilled pores exists in the PFM-B composite, as shown in Figure 3(c). Figure 5 shows the SEM micrographs of $B_4C$ and the fracture surface of $B_4C$/paraffin. The $B_4C$ particles have great surface wettability of paraffin. The

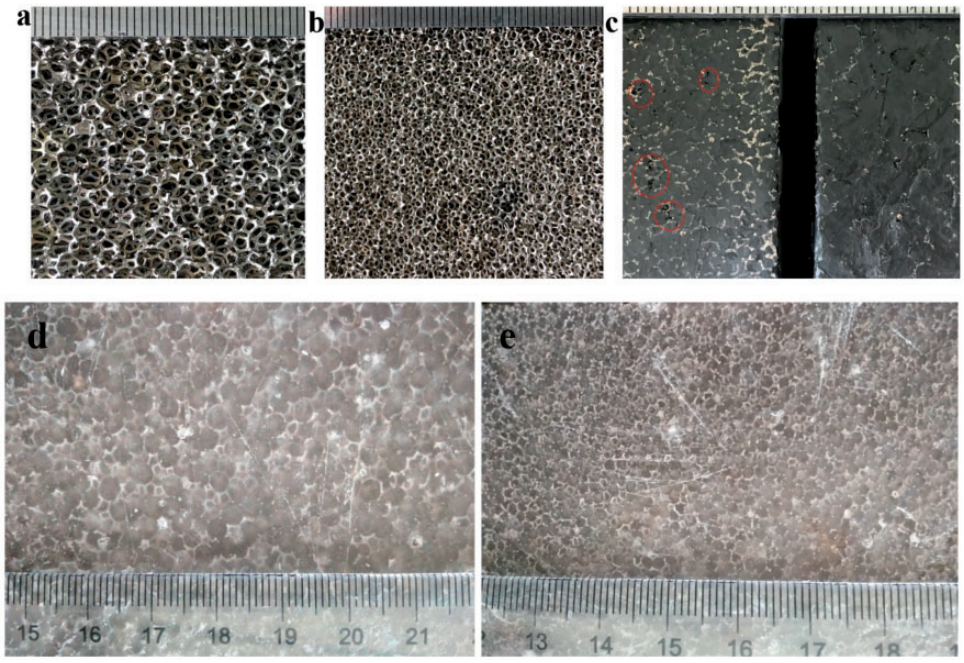


**Figure 3.** Images of (a) Ni foams with pore size of 6 PPI, (b) Ni foams with pore size of 12 PPI, (c) PFM-B composite, (d) paraffin/Ni foam composite with pore size of 6 PPI, and (e) paraffin/Ni foam composite with pore size of 12 PPI.

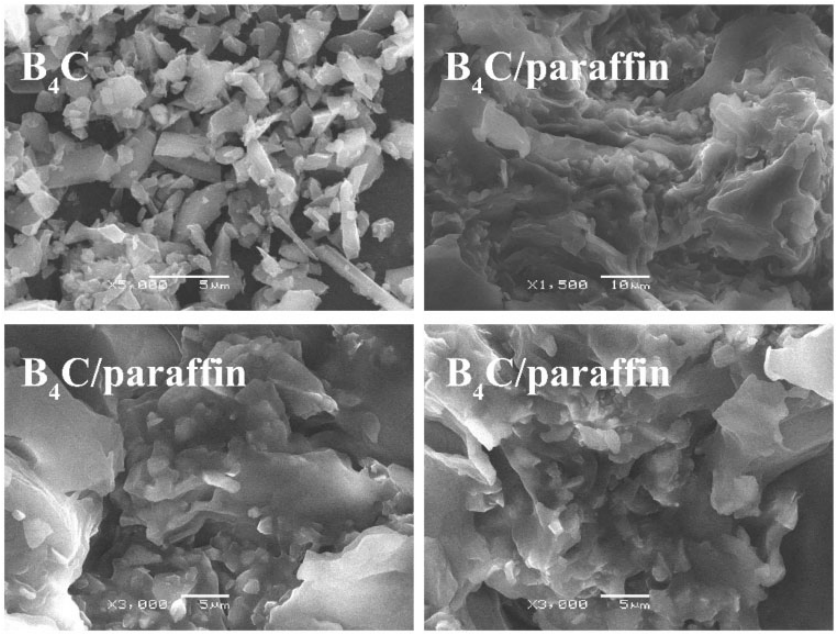


**Figure 4.** SEM micrographs of the fractured surface of boron carbide/paraffin and $B_4C$ powders.

powder was embedded in the laminar structure of paraffin uniformly. There are almost no agglomerate particles observed in the fracture surface. The impregnation ratio of $B_4C$/paraffin is much smaller than that of paraffin because the viscosity and melt flow resistance of $B_4C$/paraffin higher than that of paraffin.

The abbreviations of composites are terms in consideration of the following rules: the first number is the pore density of nickel foams, F stands for nickel foams,

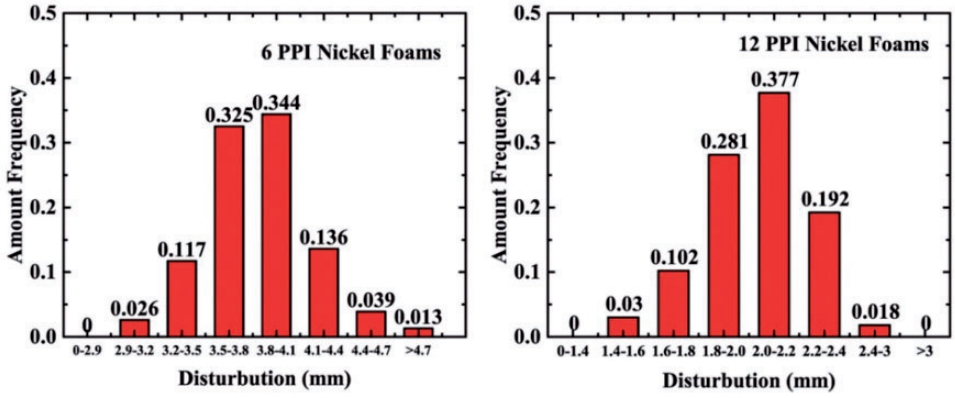


**Figure 5.** The distribution of cell size.

**Table 2.** Abbreviations of samples, density, and filling ratio of materials.

| Abbreviations of samples | Density | Filling ratio |
|---|---|---|
| 12F-BP-0.045 | 1.521 | 0.90 |
| 6F-BP-0.045 | 1.618 | 0.92 |
| 12F-BP-0.065 | 1.732 | 0.89 |
| 12F-P-0.045 | 1.251 | 0.98 |
| 6F-P-0.45 | 1.255 | 0.99 |
| 6F-0.045 | 0.4 | – |
| 12F-0.045 | 0.4 | – |
| P | 0.887 | – |
| BP | 1.356 | – |

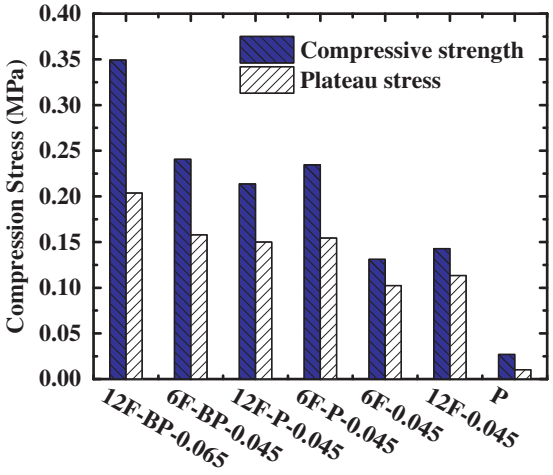


**Figure 6.** Compression strength and plateau stress.

followed by the type of fillers. BP means that the filler is borated paraffin, and P is paraffin. The nomenclature is completed with another number which represents the relative density of nickel foams.

The relative density of nickel metal with different pore sizes and the average values of the impregnation ratios of the composite calculated with equations (1) and (2), respectively, are shown in Table 2. The impregnation ratio did not reach 100% because the outer paraffin was solidified first during the cooling process, and the inner paraffin was solidified subsequently. Given that the density of pure paraffin in solid state is larger than that in liquid state, the inner paraffin was inevitably shrunk slightly during the cooling process, which led to the formation of a small cavity inside the composite. Hence, the impregnation ratio was less than 100%.[18]

Five compositions with different parameters were designed as 12 PPI open-cell Ni foams (relative density of 0.045) filled with $B_4C$/paraffin, 6 PPI open-cell Ni foams (relative density of 0.045) filled with $B_4C$/paraffin, 12 PPI open-cell Ni foams (relative density of 0.065) filled with $B_4C$/paraffin, 12 PPI open-cell Ni foams (relative density of 0.045) filled with paraffin, and 6 PPI open-cell Ni foams (relative density of 0.045) filled with paraffin.

## *Compression properties*

Figure 6 shows the compressive strength, $\sigma$, and plateau stress, $\sigma_{pl}$, of the samples. Plateau stress, which is the average of two distinguished strain ratios (10% and 40%), was selected as the limit.[23] The compressive strength of the composite increased 0.4 times that of nickel foams because of the synergistic reinforcement of paraffin and nickel foams.[24] A small difference in $\sigma_{pl}$ between samples 12F-P-0.045 and 6F-P-0.045 was observed, whereas sample 12F-P-0.045 had twice the pore density of 6F-P-0.045. The difference in pore density did not exert a major effect on shielding behavior under the condition of similar relative density. Sample

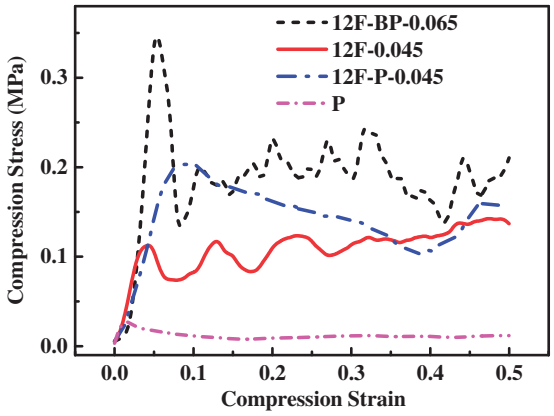


**Figure 7.** Compression tests on 12 PPI nickel foams with and without the different fillers.

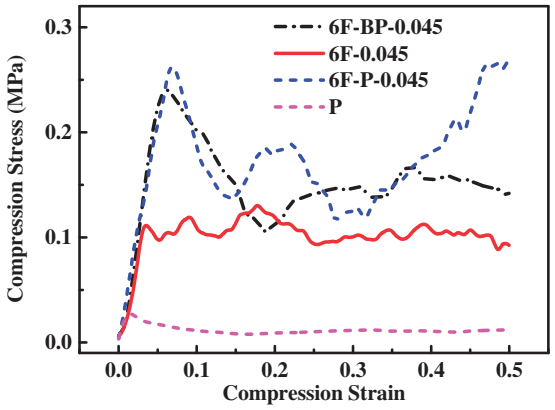


**Figure 8.** Compression tests on 6 PPI nickel foams with and without the different fillers.

12F-BP-0.065 had the highest $\sigma$ and $\sigma_{pl}$ values. A high relative density means thick nickel coating. Therefore, a thicker nickel coating of nickel foams result in better mechanical property of composite.

The engineering stress–engineering strain curves of the nickel foams (6 PPI), PFM (6 PPI), PFM-B (6 PPI), and paraffin are shown in Figure 7. The compressive curves of nickel foams (12 PPI), PFM (12 PPI), PFM-B (12 PPI), and paraffin are shown in Figure 8. The stress–strain curves can be divided into three regions, namely the initial linear elasticity, plateau and densification regions.[23,25,26] All the specimens appeared to undergo the initial linear elasticity region of their stress–strain curves.[21] Just after the elastic region, most of the curves show fluctuation in stress, the fluctuation of stress–strain curves represent localized crush and deformation spread to the rest of specimen as the compression test progressed.[21,25] The curves of composite samples show different shape in this regions, because of the heterogeneity of the composites.[26]

In Figures 7 and 8, except for the curves of 6F-P-0.045, no obvious densification regions appear until the stress reaches to 0.5. It is reasonable because the typical densification regions begin at strain up to 0.5–0.6.[27,28] Given that the curves of 6F-P-0.045 and 6F-BP-0.045 are almost similar, the addition of $B_4C$ exerted a limited effect on mechanical behavior. Meanwhile, the fillers caused a sharp increase in yield strength, but the stress of composites decreased faster than that of nickel foams after the yield point. This result is due to the condition that fillers are supposed to decrease the stress concentration of nickel foams in the compressive test, but the failure of the interface bonding between the nickel and paraffin destroyed the stress transfer at the interface after the yield point.

**Table 3.** Neutron transmittance.

| Material (20 mm) | Transmittance | Error |
|---|---|---|
| P | 0.9360 | 0.00909 |
| BP | 0.7770 | 0.04205 |
| 6F-P-0.045 | 0.9106 | 0.02410 |
| 6F-BP-0.045 | 0.7163 | 0.06545 |
| 12F-BP-0.045 | 0.7216 | 0.04512 |
| 12F-P-0.045 | 0.9425 | 0.01761 |
| 12F-BP-0.065 | 0.7509 | 0.06545 |

## *Test and simulation of neutron radiation-shielding properties*

The neutron transmission factor, $I/I_0$, was used to assess neutron-shielding properties through an experiment and simulation. $I_0$ and I are the intensities of the incident neutron beam and neutron beam transmitted through the thickness direction of the sample composites, respectively. Table 3 presents the neutron flux attenuation properties of the 20 mm-thick PFM-B and PFM composites. A small difference was observed between the paraffin and PFM or between PFM-B and $B_4C$/paraffin. The neutron-shielding capability of the composite approximated that of the fillers because the mass fraction of nickel in the composite is much less than that of the fillers, as indicated in simulation neutron spectrums of Figure 9.

The experimental and simulation results on neutron transmittance as a function of thickness under the condition of Am–Be neutron source are plotted in Figures 10 and 11. Neutron transmittance approximately and linearly decreased with increasing thickness of PFM-B or PFM. The PFM composite with a thickness of 8 cm had an $I/I_0$ value of 54.1%, and the

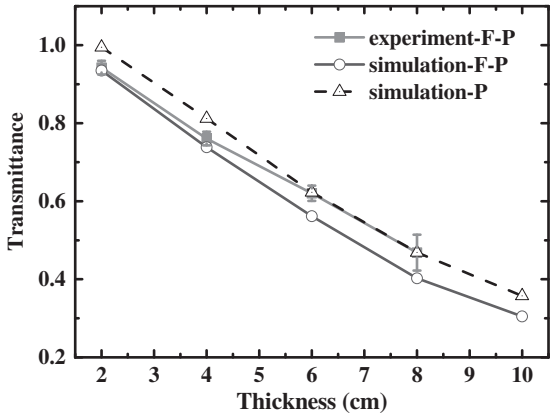


**Figure 9.** Comparison of experimental and theoretical transmission curves for PFM and boron carbide/paraffin.

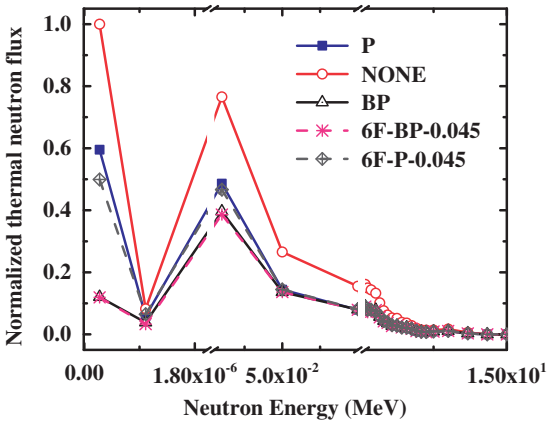


**Figure 11.** Simulative neutron spectrum of shielding experiment.

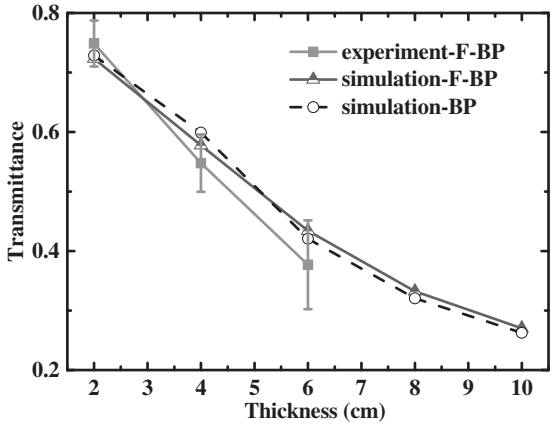


**Figure 10.** Comparison of experimental and theoretical transmission curves for PFM-B and boron carbide/paraffin.

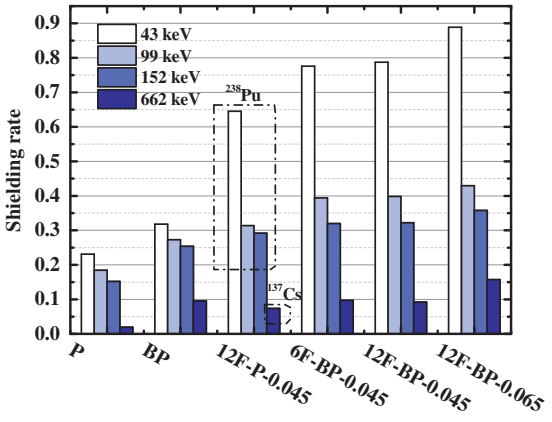


**Figure 12.** Shielding rates of gamma rays.

PFM-B composite with a thickness of 6 cm had an $I/I_0$ value of 37.6%. The experimental results are in good agreement with the simulation ones, and the difference was within the margin of error. In Figure 11, neutron transmission for experimental-F-BP is lower than those for the simulation. The viscosity of the melt paraffin was very low, $B_4C$ particle falls unavoidably at filling and cooling process. The concentration of $B_4C$ was slightly increased in the direction of gravity. The overflowed top layer filler with lower $B_4C$ concentration was chip off in the last step of preparation, thus the concentration of $B_4C$ was slightly higher than 30%. Furthermore, if the filling rate is not 100%, then the real concentration of $B_4C$ cannot be calculated exactly. In the simulation model, the concentration of $B_4C$ was set to 30%, and the density and filling rate of fillers were set according to test result (as shown in Table 2). That is the reason why the neutron transmission experimental-F-BP is lower than those of simulation.

## *Shielding effect of secondary gamma rays*

Considering the experiment condition and the destruction to the gamma ray detector by neutron, the secondary gamma ray-shielding effect was measured by a gamma photon transmission experiment at energies of 43, 99, 152, and 662 keV. Figure 12 presents the gamma ray shielding rates for all samples at a thickness of 20 mm. The shielding rates for PFM and PFM-B are significantly higher than those of paraffin and $B_4C$/paraffin, respectively. Nickel foams showed a large difference in gamma shielding rate compared with pure paraffin and $B_4C$/paraffin. Sample 6F-BP-0.045 had almost the same shielding rate as sample 12F-BP-0.045, so pore density exerted no obvious influence on gamma ray in the condition of similar relative density. Sample 12F-BP-0.065 had a higher shielding rate than sample 12F-BP-0.045 at large relative density. Secondary gamma ray attenuation can be increased by improving the relative density of the composite of nickel foams.

## Conclusions

PFM and PFM-B neutron-shielding composites with different structural parameters were fabricated through electrodeposited nickel coating and impregnation treatment. PFM and PFM-B obtained 40% higher mechanical property than nickel foams. The Am–Be source neutron transmittance experiment and gamma photon transmittance test indicated that PFM and PFM-B had a similar neutron shielding rate as their fillers. However, PFM and PFM-B had a significantly higher secondary gamma shielding rate compared with paraffin and $B_4C$/paraffin. Enhancing the structural relative density can improve the mechanical property and secondary gamma ray shielding capability. A successful model that links the observed material properties and microstructure was developed to predict the neutron-shielding efficiency of open-cell Ni foams with filler. Compounding of open-cell Ni foams with paraffin resulted in a remarkable improvement in the reliability of shielding materials and expanded the application range. Paraffin is mostly used as neutron-shielding material at room temperature. But paraffin nickel foams' composite material can retain the mechanical strength after softening point of paraffin. This research provides valuable information on optimizing the combination of open-cell foams and high-hydrogen materials as well as developing multilayer radiation protective structures to achieve ideal performance with minimum density and thickness. The fillers with high melting point such as epoxy resin and polyethylene could be studied for higher temperature work condition in the future.

### Acknowledgements

We thank Guangbin Ji for help during preparation of nickel foams. Feida Chen contributed equally to this work and should be considered co-first author.

### Declaration of Conflicting Interests

The author(s) declared no potential conflicts of interest with respect to the research, authorship, and/or publication of this article.

### Funding

The author(s) disclosed receipt of the following financial support for the research, authorship, and/or publication of this article: This work was supported by the Foundation of Graduate Innovation Center in NUAA (Grant No. kfjj20160604, Grant No. kfjj20170609), the Fundamental Research Funds for the Central Universities (Grant No. NJ20150021), Priority Academic Program Development of Jiangsu Higher Education Institutions.

### References

1. Hayashi T, Tobita K, Nakamori Y, et al. Advanced neutron shielding material using zirconium borohydride and zirconium hydride. *J Nucl Mater* 2009; 386–388: 119–121.
2. Li ZH, Chen SY, Nambiar S, et al. PMMA/MWCNT nanocomposite for proton radiation shielding applications. *Nanotechnology* 2016; 27: 10.
3. Jun J, Kim J, Bae Y, et al. Enhancement of dispersion and adhesion of B4C particles in epoxy resin using direct ultrasonic excitation. *J Nucl Mater* 2011; 416: 293–297.
4. Kim J, Lee B-C, Uhm YR, et al. Enhancement of thermal neutron attenuation of nano-B4C, -BN dispersed neutron shielding polymer nanocomposites. *J Nucl Mater* 2014; 453: 48–53.
5. Moon J and Yi S. Mechanical properties and thermal neutron shielding efficiency of high B amorphous ribbons in the Fe-B-Mo-Cr system. *Met Mater – Int* 2016; 22: 825–830.
6. Ozdemir T, Akbay IK, Uzun H, et al. Neutron shielding of EPDM rubber with boric acid: mechanical, thermal properties and neutron absorption tests. *Prog Nucl Energy* 2016; 89: 102–109.
7. Morioka A, Sakurai S, Okuno K, et al. Development of 300°C heat resistant boron-loaded resin for neutron shielding. *J Nucl Mater* 2007; 367–370: 1085–1089.
8. Jin-Ju P, Sung-Mo H, Min-Ku L, et al. Enhancement in the microstructure and neutron shielding efficiency of sandwich type of 6061Al-B4C composite material via hot isostatic pressing. *Nucl Eng Des* 2015; 282: 1–7.
9. Fletcher A and Gupta MC. Mechanical properties of elastomer nanocomposites for electromagnetic interference shielding applications. *J Compos Mater* 2014; 48: 1261–1276.
10. Dixit T and Ghosh I. Radiation heat transfer in high porosity open-cell metal foams for cryogenic applications. *Appl Thermal Eng* 2016; 102: 942–951.
11. Ibrahim MA. Heat generation and corresponding rise in temperature due to absorption of thermal neutrons in several shielding materials. *Ann Nucl Energy* 2002; 29: 1131–1136.
12. Ryan S and Christiansen EL. Hypervelocity impact testing of advanced materials and structures for micrometeoroid and orbital debris shielding. *Acta Astronaut* 2013; 83: 216–231.
13. Bhingardive V, Sharma M, Suwas S, et al. Polyvinylidene fluoride based lightweight and corrosion resistant electromagnetic shielding materials. *RSC Adv* 2015; 5: 35909–35916.
14. Yiou S, Cantwell W, Mines R, et al. Low-velocity impact performance of lattice structure core based sandwich panels. *J Compos Mater* 2014; 48: 3153–3167.
15. Chen S, Bourham M and Rabiei A. Neutrons attenuation on composite metal foams and hybrid open-cell Al foam. *Radiat Phys Chem* 2015; 109: 27–39.
16. Chen S, Bourham M and Rabiei A. Attenuation efficiency of X-ray and comparison to gamma ray and neutrons in composite metal foams. *Radiat Phys Chem* 2015; 117: 12–22.
17. Badiche X, Forest S, Guibert T, et al. Mechanical properties and non-homogeneous deformation of open-cell nickel foams: application of the mechanics of cellular

solids and of porous materials. *Mater Sci Eng A – Struct Mater Prop Microstruct Process* 2000; 289: 276–288.
18. Xiao X, Zhang P and Li M. Preparation and thermal characterization of paraffin/metal foam composite phase change material. *Appl Energy* 2013; 112: 1357–1366.
19. Devivier C, Tagliaferri V, Trovalusci F, et al. Mechanical characterization of open cell aluminium foams reinforced by nickel electro-deposition. *Mater Des* 2015; 86: 272–278.
20. Tan PJ, Reid SR and Harrigan JJ. On the dynamic mechanical properties of open-cell metal foams – a re-assessment of the 'simple-shock theory'. *Int J Solids Struct* 2012; 49: 2744–2753.
21. Ho NSK, Li P, Raghavan S, et al. The effect of slurry composition on the microstructure and mechanical properties of open-cell Inconel foams manufactured by the slurry coating technique. *Mater Sci Eng A – Struct Mater Prop Microstruct Process* 2017; 687: 123–130.
22. Chai H, Tang XB, Ni MX, et al. Preparation and properties of flexible flame-retardant neutron shielding material based on methyl vinyl silicone rubber. *J Nucl Mater* 2015; 464: 210–215.
23. Szlancsik A, Katona B, Bobor K, et al. Compressive behaviour of aluminium matrix syntactic foams reinforced by iron hollow spheres. *Mater Des* 2015; 83: 230–237.
24. Campbell JE, Suralvo M, Hibbard GD, et al. Foamed core microtruss nanocrystalline Ni cellular hybrids. *J Compos Mater* 2012; 46: 63–70.
25. Kishimoto S, Wang Q, Tanaka Y, et al. Compressive mechanical properties of closed-cell aluminum foam-polymer composites. *Compos Pt B – Eng* 2014; 64: 43–49.
26. Belhadj A-E, Gavrus A, Bernard F, et al. Mechanical and numerical analysis concerning compressive properties of tin-lead open-cell foams. *J Mater Eng Perform* 2015; 24: 4140–4155.
27. Jung A, Pullen AD and Proud WG. Strain-rate effects in Ni/Al composite metal foams from quasi-static to low-velocity impact behaviour. *Compos Pt A – Appl Sci Manuf* 2016; 85: 1–11.
28. Campbell JE, Forte F, Hibbard GD, et al. Periodic cellular metal/polyurethane foam hybrid materials. *J Compos Mater* 2009; 43: 207–216.